J. Fluid Mech. (2008), *vol.* 598, *pp.* 81–105.
doi:10.1017/S0022112007000067 Printed in the United Kingdom

Structure formation in homogeneous freely decaying rotating turbulence

P. J. STAPLEHURST[1], P. A. DAVIDSON[1] AND S. B. DALZIEL[2]

[1]Department of Engineering, University of Cambridge, Trumpington Street, Cambridge CB2 1PZ, UK

[2]Department of Applied Mathematics and Theoretical Physics, University of Cambridge, Wilberforce Rd, Cambridge CB3 0WA, UK

(Received 24 May 2007 and in revised form 29 October 2007)

One of the most striking features of rotating turbulence is the inevitable appearance of large-scale columnar structures. Whilst these structures are frequently observed, the processes by which they are created are still poorly understood. In this paper we consider the emergence of these structures from freely decaying, rotating turbulence with $Ro \sim 1$. Our study follows the conjecture by Davidson, Staplehurst & Dalziel (*J. Fluid Mech.*, vol. 557, 2006, p. 135) that the structure formation may be due to linear inertial wave propagation, which was shown to be consistent with the growth of columnar eddies in inhomogeneous turbulence. Here we extend that work and consider the case of homogeneous turbulence.

We describe laboratory experiments where homogeneous turbulence is created in a rotating tank. The turbulence is generated with $Ro \sim 1$, and as the energy decays, the formation of columnar vortices is observed. The axial growth of these columnar structures is then measured using two-point correlations and in all cases the results are consistent with structure formation via linear inertial wave propagation. In particular, we obtain a self-similar collapse of the two-point correlations when the axial coordinate is normalized by Ωtb, where b is a measure of the integral scale in the horizontal plane and Ω is the rotation rate. Although our results do not exclude the possibility of significant nonlinear dynamics, they are consistent with the conjecture of Davidson *et al.* (2006) that linear dynamics play a strong guiding hand in structure formation.

1. Introduction

We consider rapidly rotating turbulence in which the fluctuating velocity, $\boldsymbol{u}$, is small in comparison with $|\boldsymbol{\Omega}|l$, where $\boldsymbol{\Omega} = \Omega \hat{\boldsymbol{e}}_z$ is the bulk rotation rate and l the integral scale of the turbulence. It is well known that such turbulence is characterized by the growth of columnar eddies aligned with the rotation axis (Hopfinger, Browand & Gagne 1982) and there has been considerable debate as to the physical mechanisms responsible for this anisotropy.

Most researchers agree that inertial waves play a crucial role in the formation of these columnar vortices, which makes them quite different to, say, the coherent vortices seen in two-dimensional turbulence. Indeed, when inertia is weak by comparison with the Coriolis force, $\boldsymbol{u} \cdot \nabla \boldsymbol{u} \ll 2\boldsymbol{u} \times \boldsymbol{\Omega}$, the motion is simply a linear superposition of inertial waves. Many theories have emerged, but typically they focus on the case of small Rossby number, $Ro = u/2\Omega l \ll 1$, and suggest that anisotropy results from a weak nonlinear coupling of inertial waves operating over a long period of time,

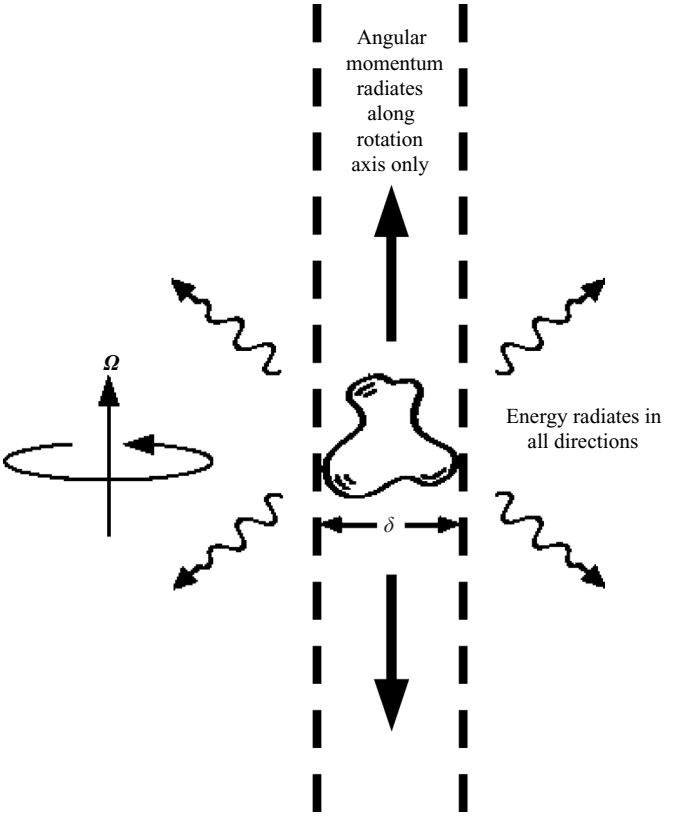

FIGURE 1. Radiation of energy from an initial blob of vorticity. While energy radiates from the vortex in all directions, the axial component of the angular momentum can only radiate along the rotation axis.

$t \sim l/u$ (see, for example, Cambon & Scott 1999). When cast in terms of Fourier space, such nonlinear interactions necessarily take the form of wavevector triads, and if we are to demand a significant nonlinear effect, despite the smallness of Ro, these wave interactions must also satisfy a resonance condition. The nonlinear theories focus, therefore, on near-resonant triad interactions and explain the growth of anisotropy in the eddy structure in terms of the slow cumulative effects of weak nonlinearity. Typical of these studies is Waleffe (1993), who proposed an explanation for the observed two-dimensionalization of rotating turbulence in terms of triadic interactions, and Cambon, Mansour & Godeferd (1997), who developed a model of spectral energy transfer in the framework of two-point closure theory.

A fundamentally different explanation for the growth of columnar vortices has been put forward by Davidson *et al.* (2006, denoted DSD hereafter). They considered unforced, decaying turbulence in which the flow evolves from an initial condition composed of a sea of spatially compact blobs of vorticity (eddies). This would be typical of a laboratory experiment in which the fluid is stirred up with a grid and then left to itself. In this theory the columnar vortices evolve simply as a result of linear wave propagation. The key point, noted in DSD, is that a blob of vorticity preferentially radiates energy and momentum along the rotation axis. The reason is as follows. Consider a blob of vorticity centred on the origin at $t = 0$, as shown in figure 1. To determine the radiation pattern for $t > 0$, we Fourier-decompose the initial

vorticity field and then, for each wavevector $\boldsymbol{k}$, calculate the associated frequency, ϖ, and group velocity, $\boldsymbol{c}_g$. For linear inertial waves, these are (Greenspan 1968),

$$\varpi = \pm 2(\boldsymbol{\Omega} \cdot \boldsymbol{k})/|\boldsymbol{k}|, \quad \boldsymbol{c}_g = \pm 2\boldsymbol{k} \times (\boldsymbol{\Omega} \times \boldsymbol{k})/|\boldsymbol{k}|^3. \tag{1.1}$$

Now an arbitrarily shaped blob of vorticity should yield an equally arbitrary spectrum of wavevectors and hence, from (1.1), we expect the corresponding group velocities to be somewhat random. We might anticipate, therefore, that the vorticity will disperse in all directions, showing no preference to evolve into a columnar eddy. However, this dispersion is subject to a powerful constraint. In particular, DSD showed that the axial components of linear and angular impulse of the initial vortex blob are confined for all time to the cylindrical region of space which circumscribes the vortex at $t = 0$. In short, the axial components of linear and angular momentum can disperse along the rotation axis only.

This constraint turns out to be crucial. Suppose that the characteristic size of the initial vortex is δ. Then, from (1.1), the fastest group velocity is directed along the rotation axis and is of the order of $c_g \sim \Omega\delta$ (where $c_g = |\boldsymbol{c}_g|$). So, after a time t, the axial component of the angular momentum is confined to a cylindrical region of volume $c_g t\delta^2 \sim \Omega t\delta^3$. This, in turn, demands that the characteristic velocity within the tangent cylinder can fall no faster than $|\boldsymbol{u}| \sim |\boldsymbol{u}_0|(\Omega t)^{-1}$, where $|\boldsymbol{u}_0|$ is the characteristic velocity at $t = 0$. Outside the tangent cylinder, however, the characteristic velocity falls as $|\boldsymbol{u}| \sim |\boldsymbol{u}_0|(\Omega t)^{-3/2}$, as the radiated energy fills a volume of order $(c_g t)^3 \sim (\Omega t\delta)^3$. (Precisely the same conclusions may be reached by the method of stationary phase.) So the restriction that angular momentum only disperses along the rotation axis ensures that the energy density is highest within the tangent cylinder and this, in turn, provides a systematic mechanism for elongating the eddies in the direction of $\boldsymbol{\Omega}$.

Of course, this theory is purely linear and relates to a flow in which $Ro \ll 1$. In order to test its relevance to rotating turbulence in which Ro is of order unity, DSD conducted an experiment. Turbulence was excited in the upper region of a rotating tank using a grid, and then the flow left to itself. Initially, Ro of the turbulence was somewhat larger than unity, but as the energy decayed, so Ro fell. When Ro reached a value of order unity, columnar eddies emerged from the turbulent cloud, propagating in the axial direction as shown schematically in figure 2.

Measurements confirmed that the columnar vortices elongate at a constant rate, and that the growth rate is proportional to the transverse scale of the vortex, δ, and to Ω:

$$l_z \sim \Omega t\delta. \tag{1.2}$$

This confirms that the vortices grow by inertial wave propagation, giving support to the idea that columnar vortex formation is a linear process, at least in the experiment described.

One weakness of this experiment, however, is that the turbulence is inhomogeneous, with the columnar vortices growing into a quiescent region. It is not immediately apparent that the same thing will happen within the interior of a homogeneous field of turbulence, particularly when $Ro \sim 1$, so that linear and nonlinear processes compete. Nevertheless, DSD speculate that, in such a case, inertial waves will continue to form columnar structures on the linear time scale of Ω^{-1}, and that these elongated eddies will provide a catalyst for nonlinear interactions as they spiral up the surrounding vorticity field. If such a situation did indeed arise, we would expect to see the integral scale l_z, defined, say, as the integral of the autocorrelation $\langle u_x(\boldsymbol{x})u_x(\boldsymbol{x} + r_\parallel \hat{\boldsymbol{e}}_z)\rangle$, to grow

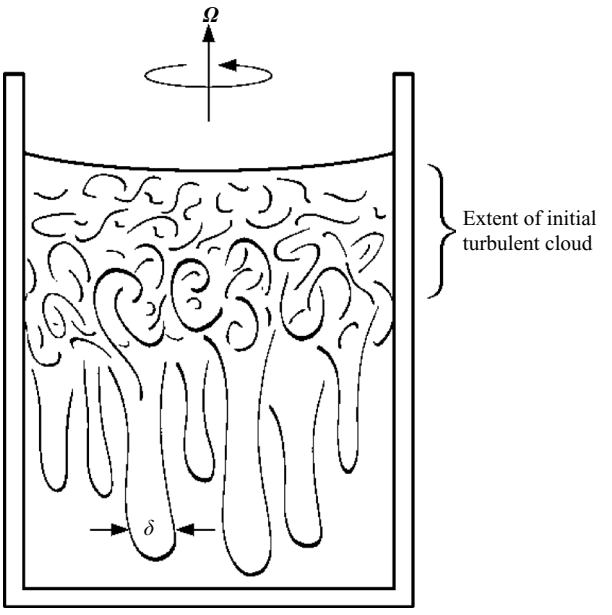

FIGURE 2. Schematic of the experiment described in DSD.

as $l_z \sim \Omega t\delta$, as the nonlinear dynamics shadow the growth of the columnar vortices. (From here on $r_\parallel$ will represent a displacement parallel to the rotation axis and $r_\perp$ a displacement perpendicular to it; a similar labelling convention will be used for other directed quantities such as wavenumber, velocity and spectral components.)

The primary purpose of this paper is to extend the study of DSD to just this situation, i.e. freely decaying, homogeneous turbulence at $Ro \sim 1$, or less. We shall see that, when Ro is somewhat smaller than unity, the vertical integral scale does indeed grow linearly in time, as $l_z \sim \Omega t\delta$.

However, we also investigate other effects of rotation. For example, we look at the asymmetry between cyclones and anti-cyclones which has been observed in many previous studies (e.g. Bartello, Metais & Lesieur 1994 and Hopfinger, Griffiths & Mory 1983) as well as the effect of rotation on energy dissipation, where we expect to see the dissipation suppressed (Jacquin *et al.* 1990).

The structure of the paper is as follows. In § 2 we ask: Are measurements of two-point autocorrelations, such as $\langle u_x(\boldsymbol{x})u_x(\boldsymbol{x}+r_\parallel\hat{\boldsymbol{e}}_z)\rangle$, sufficient to confirm or reject the hypothesis that columnar vortices form by linear wave propagation? We shall see that these correlations do indeed contain sufficient information to test the hypothesis. Next, in § 3 and § 4, we describe an experiment in which just such autocorrelations are measured, where $Ro \sim 1$ and the turbulence is homogeneous. We show that the experiments suggest $l_z \sim \Omega t\delta$, which is consistent with columnar vortex formation by linear inertial waves. Further details of the experiment are described in § 5, such as the relative dominance of cyclones and anti-cyclones, and the effect of rotation on energy dissipation. In line with other researchers, we find a dominance of cyclones, and that rotation inhibits energy dissipation. While the later effect is readily rationalized in terms of a partial two-dimensionalization of the flow, the reason for the dominance of cyclones is still poorly understood, with competing explanations being offered by Bartello *et al.* (1994) and Gence & Frick (2001).

2. Two-point correlations in homogeneous, rotating turbulence

Much of the experimental data to be presented in the subsequent sections relates to two-point autocorrelations, such as two-point vorticity measurements, taken in turbulence for which Ro is small but finite. As a prelude to discussing these data, it is natural to ask what kind of information we might expect to find in such correlations in the limit of small Ro. The point is this: the redistribution of energy and momentum by linear wave propagation is all about coordinating the phases of the various wave modes present, so that the location in space where the modes reinforce each other, rather than cancel, propagate with the group velocity (Lighthill 1978). Thus the reshaping of a vortex through the radiation of linear waves, $A\cos(\boldsymbol{k}\cdot\boldsymbol{x}-\varpi t)$, depends crucially on phase information, $\phi=\varpi t$, and it is well known that such information is almost entirely absent in an autocorrelation (Bracewell 1986). This is an inevitable consequence of the autocorrelation theorem. There is a danger, therefore, that two-point autocorrelations might be unable to detect the changes in eddy morphology caused by linear dynamics. If that were to be the case, then they would represent a poor diagnostic, blind to the very processes which interest us.

It turns out, however, that the autocorrelations do retain a minimal amount of phase information, ϕ, and this is just sufficient for us to track the formation and growth of columnar eddies by linear wave propagation. (We stress that the phase information we are referring to here is $\phi=\varpi t$, not the phase in wavenumber space.) The purpose of this section is to show exactly what kind of information is retained by the autocorrelations, thus enabling us to interpret the experimental data presented in § 4.

Consider the case where $Ro\ll 1$, so that $\boldsymbol{u}\cdot\nabla\boldsymbol{u}$ can be neglected on time scales of order Ω^{-1}. Let us start by calculating the spectral tensor, $\Phi_{ij}(\boldsymbol{k},t)$. If $\hat{\boldsymbol{u}}$ is the Fourier transform of $\boldsymbol{u}$, then the transformed equation of motion yields

$$\partial^2\hat{\boldsymbol{u}}/\partial t^2+\varpi^2\hat{\boldsymbol{u}}=0, \tag{2.1}$$

where ϖ is given by (1.1) and we have neglected viscosity. On integrating (2.1), we find

$$\hat{\boldsymbol{u}}(\boldsymbol{k},t)=\hat{\boldsymbol{u}}^{(0)}\cos\varpi t-(\boldsymbol{k}\times\hat{\boldsymbol{u}}^{(0)}/k)\sin\varpi t, \tag{2.2}$$

where $\hat{\boldsymbol{u}}^{(0)}$ is the initial distribution of $\hat{\boldsymbol{u}}$, $k=|\boldsymbol{k}|$ and we have used $\partial\boldsymbol{\omega}/\partial t=2\boldsymbol{\Omega}\cdot\nabla\boldsymbol{u}$ to relate $\partial\hat{\boldsymbol{u}}^{(0)}/\partial t$ to $\hat{\boldsymbol{u}}^{(0)}$. From this we can calculate the spectral tensor, which is the transform of the two-point velocity correlation, $Q_{ij}=\langle u_iu_j'\rangle$. It is readily confirmed that (DSD)

$$\begin{aligned}2\Phi_{ij}=\Phi_{ij}^{(0)}+k^{-2}\varepsilon_{ipq}\varepsilon_{jmn}k_pk_m\Phi_{qn}^{(0)}+\left[\Phi_{ij}^{(0)}-k^{-2}\varepsilon_{ipq}\varepsilon_{jmn}k_pk_m\Phi_{qn}^{(0)}\right]\cos 2\varpi t\\ -k^{-1}\left[\varepsilon_{imn}k_m\Phi_{nj}^{(0)}+\varepsilon_{jpq}k_p\Phi_{iq}^{(0)}\right]\sin 2\varpi t,\end{aligned} \tag{2.3}$$

and, if the turbulence is statistically axisymmetric, this yields

$$\Phi_{\parallel}=\Phi_{\parallel}^{(0)}+\left[\left(k_\perp^2/2k^2\right)\Phi_{ii}^{(0)}-\Phi_{\parallel}^{(0)}\right](1-\cos 2\varpi t), \tag{2.4}$$

$$\Phi_{\perp}=\Phi_{\perp}^{(0)}-\left[\left(k_\perp^2/2k^2\right)\Phi_{ii}^{(0)}-\Phi_{\parallel}^{(0)}\right]\left(1-\cos 2\varpi t\right), \tag{2.5}$$

where $\Phi_{\parallel}=\Phi_{zz}$, $\Phi_{\perp}=\Phi_{xx}+\Phi_{yy}$ and $k_\perp^2=k_x^2+k_y^2$.

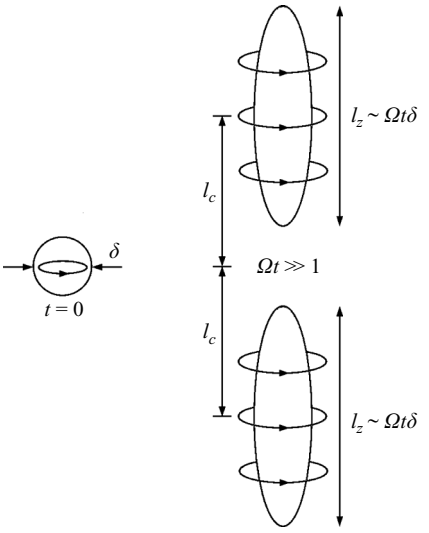

FIGURE 3. Conversion of a Gaussian eddy into a pair of columnar vortices by linear inertial wave propagation.

From (2.3) we see that $\Phi_{ii} = \Phi_{ii}^{(0)}$. Moreover, in the particular case where $\Phi_{ij}^{(0)}$ is isotropic we have the stronger condition, $\Phi_{ij} = \Phi_{ij}^{(0)}$.† The fact that Φ_{ij} cannot evolve for isotropic initial conditions provides a powerful reminder that a great deal of phase information has been removed from (2.3) $\rightarrow$ (2.5). Nevertheless, there is some residual information in the form of $\cos 2\varpi t$ on the right of (2.4) and (2.5), and it turns out that this is enough to track the formation of columnar eddies by linear wave propagation, as we now show.

To focus thoughts, let us consider a simple, if somewhat contrived, initial condition. Suppose that, at $t = 0$, we have a sea of Gaussian eddies of the form

$$\boldsymbol{u} = \pm \Lambda r \exp[-2(r^2 + z^2)/\delta^2]\hat{\boldsymbol{e}}_\theta, \tag{2.6}$$

which are randomly but uniformly distributed in space. (Here r, θ, z are polar coordinates.) Each of these eddies will immediately radiate energy through inertial waves, causing a change in their shape. Focusing on just one eddy we find that, although there is some lateral radiation of energy, the dominant structure at large Ωt is a pair of columnar vortices of length $l_z \sim \Omega t\delta$, whose centres propagate along the rotation axis at a rate $l_c \sim \Omega t\delta$, as shown in figure 3. (The details are spelt out in DSD.) By superposition, each vortex in our initial condition will behave in this way and the question at hand is whether there is enough residual phase information in (2.4) and (2.5) to detect this change in eddy morphology.

Now it is readily confirmed that, at $t = 0$, the spectral tensor corresponding to this random sea of Gaussian eddies is (Townsend 1976; Davidson 2007)

$$\Phi_\perp^{(0)} = A k_\perp^2 \exp[-k^2\delta^2/4], \quad A = \langle \boldsymbol{u}^2 \rangle \delta^5 / 32\pi^{3/2}, \tag{2.7}$$

† Of course, in laboratory experiments at $Ro \sim 1$, isotropic initial conditions cannot be created as the Coriolis force influences the dynamics from the outset.

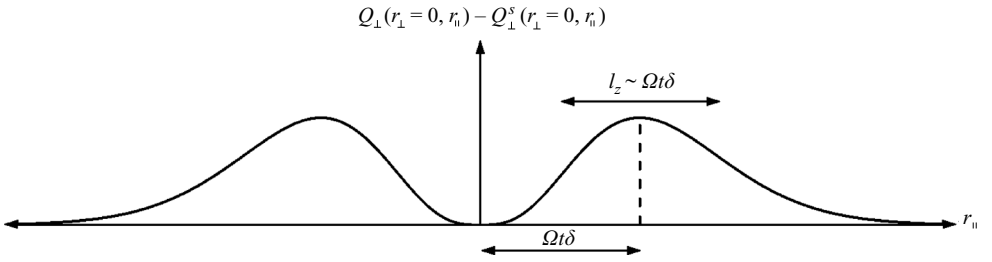

FIGURE 4. Schematic illustration of the time-dependent term in (2.11). Note that the area under the curve is constant.

and the corresponding two-point correlation is

$$Q_\perp^{(0)}(\boldsymbol{r}) = \langle \boldsymbol{u}_\perp^{(0)}(\boldsymbol{x}) \cdot \boldsymbol{u}_\perp^{(0)}(\boldsymbol{x}+\boldsymbol{r}) \rangle = \langle \boldsymbol{u}^2 \rangle [1 - (r_\perp/\delta)^2] \exp\left[-\left(r_\perp^2 + r_\parallel^2\right)/\delta^2\right]. \tag{2.8}$$

Of course, $\Phi_\parallel^{(0)}$ and $Q_\parallel^{(0)}$ are both zero. Using (2.5) to find $\Phi_\perp$, and taking the inverse transform, yields, after a little algebra,

$$Q_\perp = Q_\perp^S(\boldsymbol{r}) + \pi A \int_0^\infty \int_0^\infty \left(k_\perp^2/k^2\right) k_\perp^3 \exp[-k^2\delta^2/4] J_0(k_\perp r_\perp) \times [\cos(k_\parallel r_\parallel - 2\varpi t) + \cos(k_\parallel r_\parallel + 2\varpi t)] \, \mathrm{d}k_\perp \mathrm{d}k_\parallel, \tag{2.9}$$

where $Q_\perp^S(\boldsymbol{r})$ is the steady component of $Q_\perp$:

$$Q_\perp^S = 4\pi A \int_0^\infty \int_0^\infty \left(1 - k_\perp^2/2k^2\right) k_\perp^3 \exp[-k^2\delta^2/4] J_0(k_\perp r_\perp) \cos(k_\parallel r_\parallel) \, \mathrm{d}k_\perp \mathrm{d}k_\parallel. \tag{2.10}$$

(Here we have taken advantage of the fact that the two-dimensional transform of an axisymmetric function simplifies to a one-dimensional Hankel transform according to

$$\int \Phi_\perp \exp\left[j\boldsymbol{k}_\perp \cdot \boldsymbol{r}\right] \mathrm{d}\boldsymbol{k}_\perp = 2\pi \int_0^\infty \Phi_\perp k_\perp J_0(k_\perp r_\perp) \, \mathrm{d}k_\perp,$$

where J_0 is the usual Bessel function.)

We shall show the precise form of (2.9) shortly. In the meantime, we note that the main characteristics of (2.9) may be exposed using a simple approximation. The integral is dominated by transverse and axial wavenumbers of order $k_\perp \sim \delta^{-1}$, $k_\parallel \sim 0$. This suggests that a reasonable approximation to (2.9) is to replace $\varpi = 2\Omega k_\parallel/k$ by $2\Omega k_\parallel/k_\perp$ in the cosines, and replace $(k_\perp^2/k^2)$ by unity at the start of the integrand. The terms involving $k_\parallel$ can then be integrated exactly, and we find

$$Q_\perp \approx Q_\perp^S(\boldsymbol{r}) + \frac{1}{2}\langle \boldsymbol{u}^2 \rangle \int_0^\infty \kappa^3 \mathrm{e}^{-\kappa^2} J_0\left(\kappa \frac{2r_\perp}{\delta}\right) \times \left\{ \exp\left[-\left(\frac{r_\parallel}{\delta} - \frac{2\Omega t}{\kappa}\right)^2\right] + \exp\left[-\left(\frac{r_\parallel}{\delta} + \frac{2\Omega t}{\kappa}\right)^2\right] \right\} \mathrm{d}\kappa, \tag{2.11}$$

where $\kappa = k_\perp\delta/2$. Equation (2.11) has the advantage over (2.9) in that it is easier to interpret. The time-dependent part of the correlation is centred on $r_\parallel \sim \pm\Omega t\delta$, and its characteristic axial length scale grows as $l_z \sim \Omega t\delta$. This is illustrated schematically in figure 4 and mimics, albeit in a statistical sense, the behaviour of individual eddies as shown in figure 3. For $\Omega t \gg 1$, (2.11) simplifies considerably. Consider $r_\parallel = 2\Omega t\delta$. Then the only contribution to (2.11) comes from wavevectors $\kappa = 1 \pm O((2\Omega t)^{-1})$, and

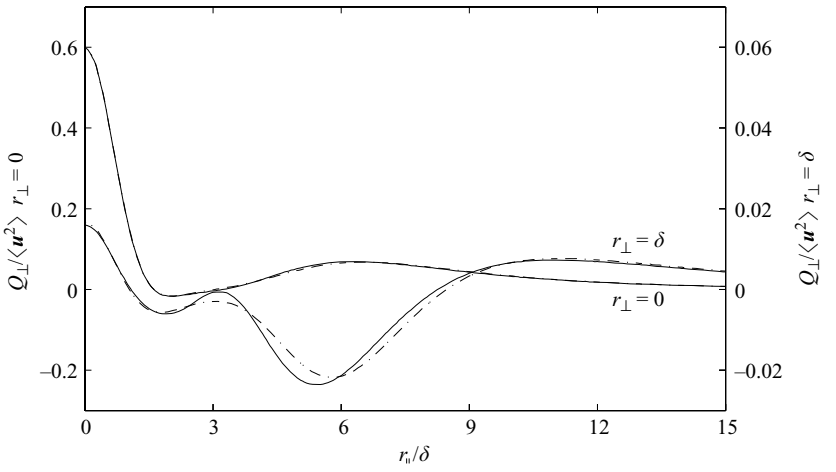

FIGURE 5. A comparison of approximation (2.11) with (2.9) at $2\Omega t = 10$ and at the radial locations $r_\perp = 0, \delta$, —, exact (2.9); $-\cdot-$, approximation (2.11). $Q_\perp$ is normalized by $\langle \boldsymbol{u}^2\rangle$.

so (2.11) integrates to give

$$Q_\perp(r) \approx \frac{\sqrt{\pi}}{2e}\langle \boldsymbol{u}^2\rangle J_0\left(\frac{2r_\perp}{\delta}\right)(2\Omega t)^{-1}, \quad r_\parallel = 2\Omega t\delta,\ \Omega t \to \infty. \tag{2.12}$$

In order to check the accuracy of approximation (2.11) we have integrated (2.9) numerically and compared (2.9) with (2.11) at $2\Omega t = 10$ and at $r_\perp = 0, \delta$ (figure 5). The two distributions are indeed similar.

Moreover, in order to verify (2.9), we have performed a simple numerical experiment in which 10^6 Gaussian eddies of the form (2.6) were randomly but uniformly distributed in a cylindrical domain of radius 10δ and length $5 \times 10^5\delta$. The flow then develops according to linear theory, and the details calculated using superposition and the fact that we know how a single Gaussian eddy evolves (DSD). The autocorrelation $Q_\perp(r_\perp = 0, r_\parallel)$ was calculated on the centreline using a volume average to substitute for the ensemble average, and the difference between the computed correlation and (2.9) was found to be always less than 5×10^{-3}, confirming (2.9).

In figure 6 we show $Q_\perp(r_\perp = 0, r_\parallel)$ calculated both from the exact solution (2.9) and the approximate solution (2.11). As expected from (2.11) the autocorrelation becomes increasingly self-similar when $r_\parallel$ is scaled by $2\Omega t\delta$.

Evidently, in this simple model problem, sufficient phase information is retained by $Q_\perp$ to track the change in eddy morphology. Note that, from (2.4), precisely the same time-dependent information is contained in $Q_\parallel$,

$$Q_\parallel \approx Q_\perp^{(0)} - Q_\perp^S - \frac{1}{2}\langle \boldsymbol{u}^2\rangle \int_0^\infty \kappa^3 \mathrm{e}^{-\kappa^2} J_0\left(\kappa\frac{2r_\perp}{\delta}\right) \times \left\{\exp\left[-\left(\frac{r_\parallel}{\delta} - \frac{2\Omega t}{\kappa}\right)^2\right] + \exp\left[-\left(\frac{r_\parallel}{\delta} + \frac{2\Omega t}{\kappa}\right)^2\right]\right\} \mathrm{d}\kappa, \tag{2.13}$$

and similar information is contained in the two-point vorticity correlation, $\langle \omega_z \omega_z'\rangle$, since

$$\langle \omega_z \omega_z'\rangle = -\nabla_\perp^2 Q_{ii} + \nabla^2 Q_\parallel = -\nabla_\perp^2 Q_\perp^{(0)} + \nabla^2 Q_\parallel. \tag{2.14}$$

The exact form of $Q_\parallel$ is compared with the approximation (2.13) in figure 7.

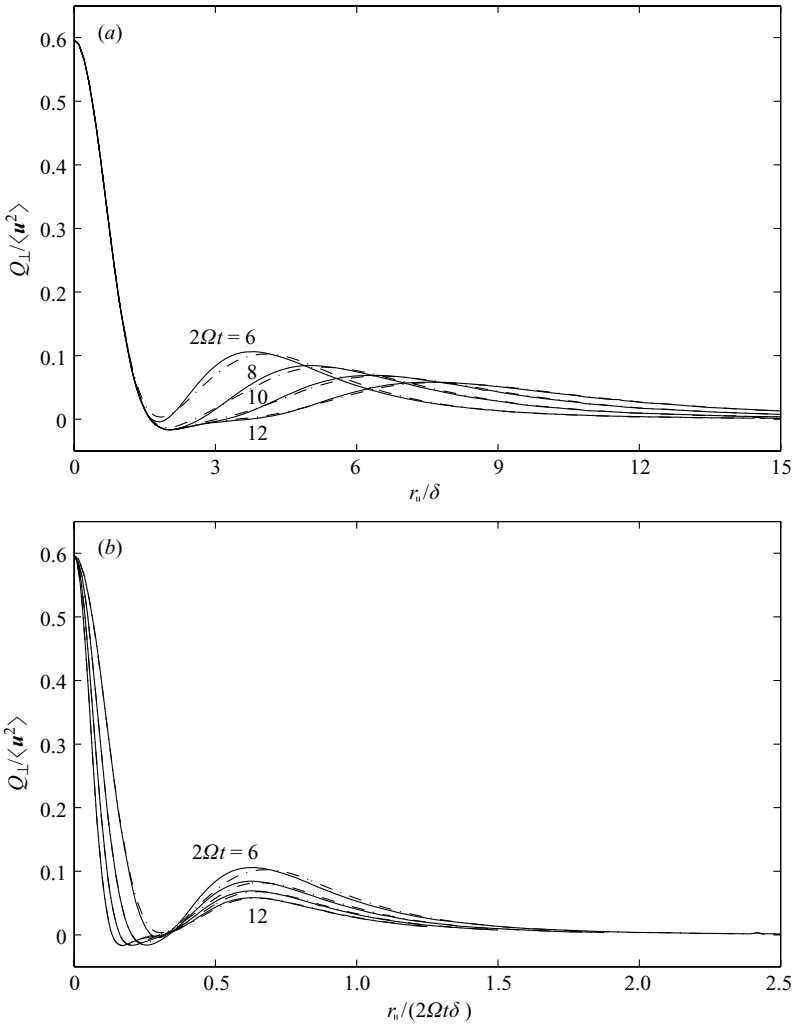

FIGURE 6. $Q_\perp(r_\perp = 0, r_\parallel)$ normalized by $\langle \boldsymbol{u}^2 \rangle$ for $2\Omega t = 6$, 8, 10 and 12: —, exact (2.9); $-\cdot-$, approximation (2.11). (*a*) $r_\parallel$ normalized by δ, (*b*) $r_\parallel$ normalized by $2\Omega t\delta$.

Now the model problem described above is somewhat contrived, designed to simplify the analysis. However, it is clear from (2.4) and (2.5), and from figure 1, that we would expect similar results for other initial conditions, provided those initial conditions are not isotropic. In particular, we would expect $r_\parallel$ to scale with $2\Omega t\delta$ for large Ωt, as shown in figures 6 and 7. If the same scaling is seen in the experiments, then this provides strong evidence that the eddies are elongating by virtue of linear wave propagation.

Finally we note that, if we define an integral scale in the usual way, as the integral of an autocorrelation, then we lose the phase information relating to the change in eddy morphology by linear wave propagation. For example,

$$\int_{-\infty}^{\infty} Q_\perp \, \mathrm{d}r_\parallel = \int_{-\infty}^{\infty} \left\{ \int \mathrm{e}^{j\boldsymbol{k}\cdot\boldsymbol{r}} \Phi_\perp \, \mathrm{d}\boldsymbol{k} \right\} dr_\parallel = 2\pi \int \mathrm{e}^{j\boldsymbol{k}_\perp \cdot \boldsymbol{r}_\perp} \Phi_\perp(\boldsymbol{k}_\perp, k_\parallel = 0) \, \mathrm{d}\boldsymbol{k}_\perp \qquad (2.15)$$

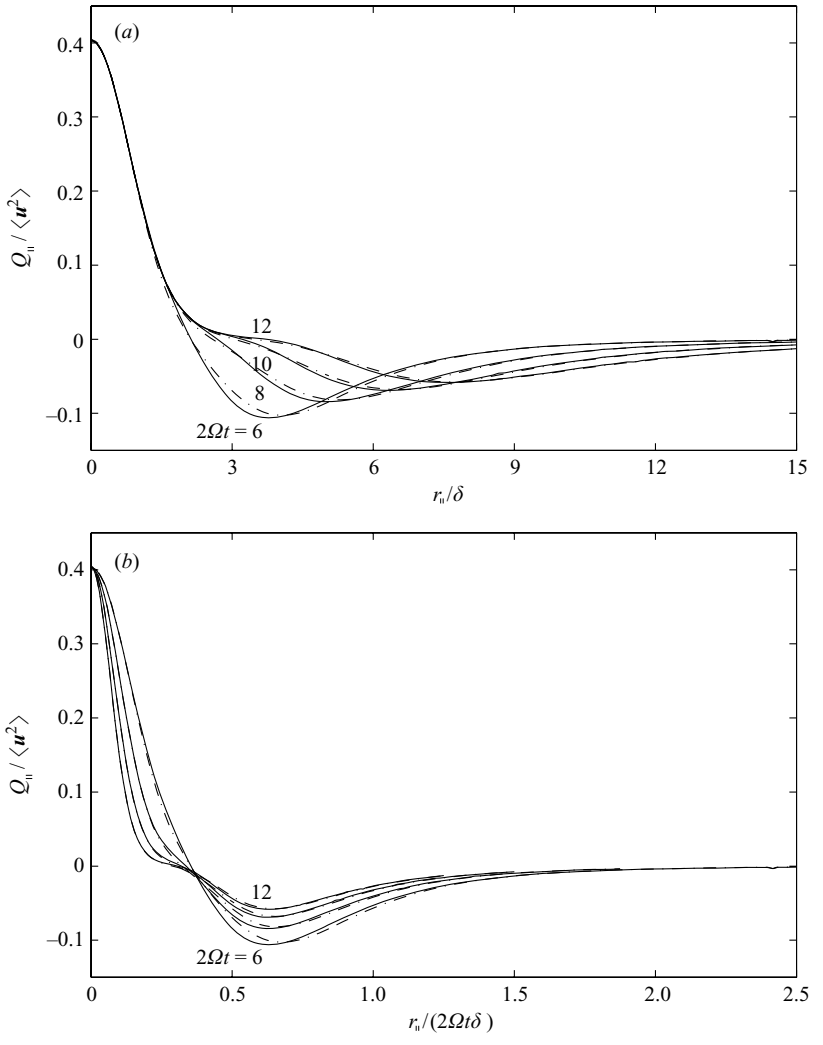

FIGURE 7. $Q_{\parallel}(r_{\perp}=0, r_{\parallel})$ normalized by $\langle \boldsymbol{u}^2 \rangle$ for $2\Omega t = 6$, 8, 10 and 12: —, exact (2.9); —·—, approximation (2.11). (*a*) $r_{\parallel}$ normalized by δ, (*b*) $r_{\parallel}$ normalized by $2\Omega t\delta$.

and hence, from (2.3),

$$\int_{-\infty}^{\infty} Q_{\perp}\, \mathrm{d}r_{\parallel} = \int_{-\infty}^{\infty} Q_{\perp}^{(0)}\, \mathrm{d}r_{\parallel} = \text{constant}. \tag{2.16}$$

This behaviour is exhibited by (2.11), where the integral of the time-dependent terms are constant, as indicated by figure 4.

Thus, for $Ro \ll 1$, the integral scale l_z, defined in the usual way as

$$l_z = \frac{1}{\langle \boldsymbol{u}_{\perp}^2 \rangle} \int_0^{\infty} Q_{\perp}(r_{\perp}=0, r_{\parallel})\, \mathrm{d}r_{\parallel}, \tag{2.17}$$

would show no tendency to elongate as $l_z \sim 2\Omega t\delta$. However, definition (2.17) is quite arbitrary, which suggests that, for $Ro \ll 1$, we should adopt a different definition of

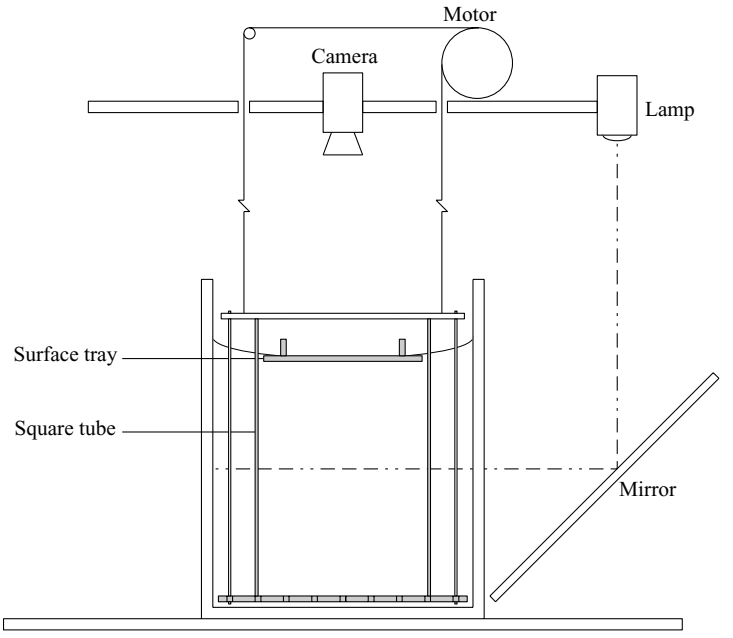

FIGURE 8. The apparatus.

the integral scale, and an obvious candidate is something like

$$L_z = \left\{ \frac{1}{\langle \boldsymbol{u}_\perp^2 \rangle} \int_0^\infty Q_\perp(r_\perp = 0, r_\parallel) r_\parallel \, \mathrm{d}r_\parallel \right\}^{1/2}, \tag{2.18}$$

which can track the elongation of the eddies in our model problem. (We note that this particular length scale is zero in isotropic turbulence.) When $Ro \sim 1$, however, it probably does not matter which definition we use. That is, if Ro is finite but somewhat less than unity, we would expect nonlinear interactions to shadow the linear dynamics as the columnar vortices spiral up the surrounding vorticity field. In such a situation, the nonlinear interactions will occur on the length scale of the columnar vortices and the axial integral scale, defined via (2.17), would indeed exhibit the scaling $l_z \sim \Omega t \delta$. We shall return to this issue shortly.

3. Experimental method

To test the relevance of our linear theory we have performed experiments on rotating turbulence with $Ro \sim 1$. The apparatus is shown schematically in figure 8. All experiments were performed in an acrylic tank, 60 cm deep and 45 cm square, which was filled with water. Turbulence was created by lowering a grid through the water at a constant velocity of $0.19\,\mathrm{m\,s^{-1}}$. To vary the largest scales of the turbulence, two geometrically similar square grids were used, with mesh sizes, M, of 32 mm and 50 mm, and a bar size of $b = M/5$.

Previous studies (e.g. McKenna & McGillis 2004 and Morize & Moisy 2006) have highlighted the problem that large-scale systematic flows can be generated between the edges of the grid and the tank walls. Here we have isolated this unwanted effect by clamping a 35-cm-square tube to the back of the grid, so that both the grid and the tube are lowered through the tank at the same time. Tests showed that in the

Symbol	Ω (rad s^{-1})	M (mm)	Re	Ro
■	0	32	83	∞
□	0	50	130	∞
◆	0.94	32	83	1.4
◇	0.94	50	130	1.0
●	1.94	32	83	0.7
○	1.94	50	130	0.5

TABLE 1. Experimental conditions.

$\Omega = 0$ case the strength of the systematic flow within the tube was reduced by a factor of around 5. A shallow tray positioned within the tube both eliminated surface waves and provided a rigid surface through which images could be recorded.

All of the apparatus is mounted on a turntable and the rotating experiments were conducted at rotation rates of $\Omega = 0.94\,\mathrm{rad\,s^{-1}}$ and $1.94\,\mathrm{rad\,s^{-1}}$. The tank rotated in an anti-clockwise direction when viewed from above. Non-rotating experiments were also conducted to compare with the rotating cases. The initial Reynolds number, $Re = ub/\nu$, and Rossby number, $Ro = u/2\Omega l$, for the different configurations are provided in table 1, where $u^2 = \langle \boldsymbol{u}^2 \rangle / 3$. Here u/l in Ro has been estimated from measurements of the integral scale root-mean-square vorticity (see § 4.2).

The turbulence was visualized using two distinct techniques. In the first, pearlescence (consisting of small reflective flakes made from fish scales) was illuminated by a lightsheet and provided a direct visualization of the structure of the turbulence, while in the second, Pliolite particles were used to obtain two-dimensional PIV measurements of the velocity field. In both cases images were captured at 27 frames per second using a 1 M pixel digital camera operating at 8 bits. A 25-cm-square region, centred on the midpoint of the tank, was recorded for a time $2\Omega t = 40$ in the rotating cases and 20 s in the non-rotating cases, where $t = 0$ corresponds to the instant when the grid passes through the centre of the tank. Figure 8 shows the configuration for the PIV experiments employing a horizontal lightsheet. For PIV experiments using a vertical lightsheet, and the pearlescence visualizations, the linear halogen light source was rotated 90° about the vertical axis. In this case the camera was positioned at the side of the turntable, viewing the flow through a front-silvered mirror mounted at 45°. For the PIV and pearlescence experiments the lightsheets were 5 mm and 10 mm thick respectively.

Pearlescence consists of individual plate-like particles which become aligned with the flow and selectively reflect the illuminating light towards an observer. Jeffery (1922) and Savas (1985) have attempted to characterize the behaviour of these particles, showing how they respond to simple strain and shear. For the purposes of our study it is sufficient to note that they tend to highlight regions of intense, persistent strain. They are therefore good for identifying large-scale, coherent structures, but are insensitive to small-scale turbulence. In our experiments it was observed that the pearlescence highlighted a range of scales that were of the order of the largest eddies in the turbulence. This is illustrated in figure 9, which shows images from the same decaying rotating turbulence experiment at two different times.

In order to obtain an objective statistical measure of the large-scale structures highlighted by the pearlescence, we focused on the fluctuations in light intensity,

$$I(\boldsymbol{x}, t) = \tilde{I}(\boldsymbol{x}, t) - \langle \tilde{I}(\boldsymbol{x}, t) \rangle, \tag{3.1}$$

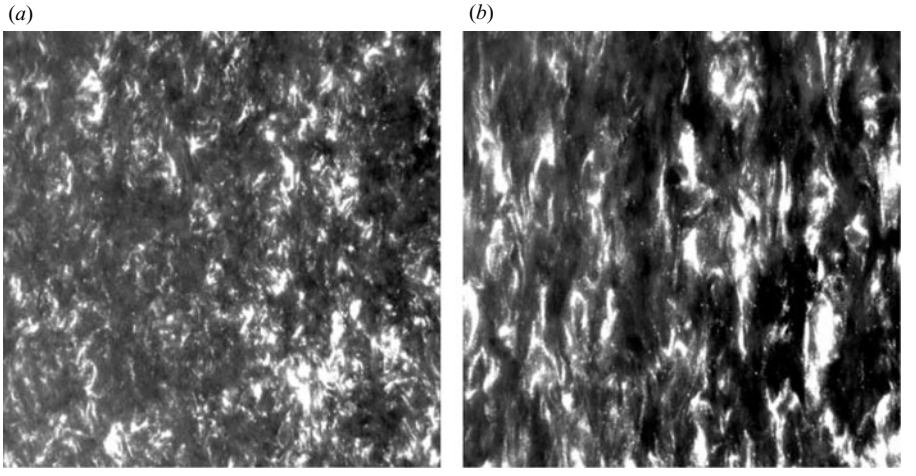

FIGURE 9. Images of the flow taken after initiation of the turbulence with $M = 32\,\mathrm{mm}$ and $\Omega = 1.94\,\mathrm{rad\,s^{-1}}$. (*a*) $2\Omega t = 14.2$, (*b*) $2\Omega t = 29.1$. The images are 25 cm square.

where $\tilde{I}$ is the recorded light intensity in a given experiment and $\langle \cdots \rangle$ is the ensemble average over 50 realizations. Two-point correlations of $I(\boldsymbol{x}, t)$ are given in § 4.1.

The pattern-matching calculations for the PIV images were performed using DigiFlow (e.g. Dalziel *et al.* 2007). The $212\,\mu\mathrm{m} \rightarrow 250\,\mu\mathrm{m}$ Pliolite particles were rendered neutrally buoyant by the addition of a small amount of salt to the water. Here the capture rate proved sufficient to accurately determine the velocities to within five mesh spaces of the descending grid. As we are interested in the large-scale structures within the turbulence, the modest frame rate and relatively large particle size were more than adequate. Tests using a laminar flow showed that we were able to measure the velocities to an accuracy of better than $\pm 4 \times 10^{-4}\,\mathrm{m\,s^{-1}}$, independent of the particle velocity for $|\boldsymbol{u}| \lesssim 2.5 \times 10^{-2}\,\mathrm{m\,s^{-1}}$. Statistical convergence was ensured through averaging over an ensemble of fifty nominally identical experiments.

To ensure a consistent treatment of any unresolved scales, we adjusted the size and spacing of the interrogation windows used in the PIV to scale with the mesh size. The net result was the accurate resolution of the structures down to the bar size, b, in all experiments. This resolution is in line with that employed by previous researchers (e.g. Morize, Moisy & Rabaud 2005 and Ruppert-Felsot *et al.* 2005).

Vorticity fields were determined as part of the sub-pixel image distortion framework used by DigiFlow. The finite resolution of the velocity measurements inevitably means the vorticity field is low-pass-filtered, discarding the highest vorticities that occur at scales smaller than the spacing between our interrogation windows. The vorticity measurements also contain a higher level of noise (around 5 % of the root-mean-square value at a given instant) than the velocity information itself. As with the pearlescence experiments, the measurements were averaged over fifty realizations, and we believe the large size of the ensemble and integral nature of the statistics makes the results robust.

From both the pearlescence images and the PIV, the change of eddy morphology within the rotating turbulence could clearly be seen. To track the growth of the columnar eddies we shall use two-point one-time correlations,

$$R^a(r_\parallel) = \frac{\langle a a' \rangle}{\langle a^2 \rangle}, \quad a' \equiv a(\boldsymbol{x} + r_\parallel \hat{\boldsymbol{e}}_z). \tag{3.2}$$

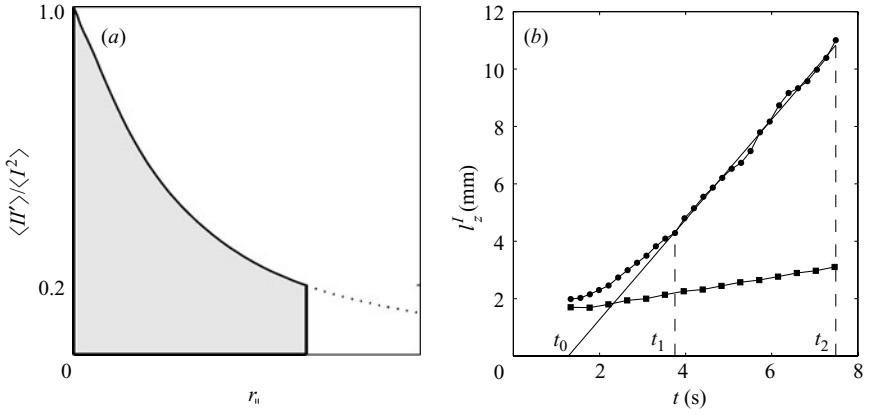

FIGURE 10. (*a*) The shaded region represents the area used to evaluate the integral scale. (*b*) The growth of the integral scale from pearlescence experiments: ■, $M = 32$ mm, $\Omega = 0$ rad s^{-1}; ●, $M = 32$ mm, $\Omega = 1.94$ rad s^{-1}.

The variable a represents either the reflected light intensity of the pearlescence, I, or the horizontal vorticity component from the PIV, ω_x. Integral scales based on $R^a\left(r_{\parallel}\right)$ are determined by

$$l_z^a = \int_0^{\beta} R^a(r_{\parallel})\, \mathrm{d}r_{\parallel}. \tag{3.3}$$

For laboratory experiments it is impractical to evaluate the integral for $\beta \to \infty$, as the measurements of $R^a(r_{\parallel})$ at large separations tend to be dominated by the weak systematic flow. Instead, we follow the strategy of previous authors and select β such that $R^a(\beta) = const$, here taken as 0.2. This is illustrated in figure 10(*a*) and gives a consistent approximation to the limit of $\beta \to \infty$ provided $R^a(r_{\parallel})$ is self-similar.

4. Statistics in a vertical plane

4.1. *Two-point correlations based on reflected light intensity*

The results from the pearlescence experiments, based on images similar to those in figure 9, will now be introduced. By using $\langle II' \rangle / \langle I^2 \rangle$, we shall see that the large-scale evolution of rotating turbulence can be characterized by two distinct periods in time. During the initial period, defined as $t < t_1$, we have $Ro \sim 1$ and so both nonlinear effects, characterized by $(\boldsymbol{u} \cdot \nabla)\boldsymbol{u}$, and the Coriolis force influence the behaviour of the fluid. During the second period, defined as $t_1 < t < t_2$, columnar eddies emerge and despite the continuing presence of nonlinearity, characteristics indicative of linear processes are observed. The values of t_1 and t_2, as well as the corresponding Rossby numbers, are given in table 2. For times greater than t_2, the presence of the weak background flow becomes significant and the measurements unreliable.

Before discussing the autocorrelations, let us focus on these two periods by considering the axial integral scale, l_z^I. Figure 10(*b*) shows the growth l_z^I for the smaller mesh of $M = 32$ mm and rotation rates of $\Omega = 0$ and 1.94 rad s^{-1}. When solid-body rotation is present it is clear that this axial length scale grows at a faster rate, corresponding to the growth of columnar eddies. The two periods for the development of the flow are also apparent. Initially, for $t < t_1$ and $Ro \sim 1$, the integral scale is a nonlinear function of time; however, at the later times of $t_1 < t < t_2$, the growth rate is

Symbol	Ω (rad s^{-1})	M (mm)	Ro ($t = t_1$)	$2\Omega t_0$	$2\Omega t_1$	$2\Omega t_2$	2Ω ($t_2 - t_1$)
◆	0.94	32	0.65	1.2	7.0	16.5	9.5
◇	0.94	50	0.42	4.0	14.0	25.5	11.5
●	1.94	32	0.38	5.0	14.2	29.1	14.9
○	1.94	50	0.37	6.8	14.6	25.7	11.1

TABLE 2. The time during which the correlations based on reflected light intensity were measured. The integral scale, l_z^I grows linearly during the interval $t_1 < t < t_2$, and t_0 is the virtual origin in time, as defined by figure 10(b). The values of Ro are based on measurements of the integral scale vorticity, with $Ro = \langle \omega_x^2 \rangle^{1/2}/2\Omega$. (See § 4.2.)

constant. The latter is consistent with inertial waves elongating the large-scale eddies which, in turn, distort the surrounding vorticity field by nonlinear interactions.

Now consider the autocorrelation curves. Figure 11(a) displays the curves that were used to produce figure 10(b). In the rotating case the curves become correlated over ever-larger distances, showing that the largest scales of the turbulence are growing in the axial direction. Furthermore, the linear development in time, which was observed in l_z^I, is also evident in the autocorrelations. This can be seen in figure 11(b), which shows the autocorrelations with $r_\parallel$ normalized by $(t - t_0)$, where t_0 is the virtual origin displayed in figure 10(b). For $t_1 < t < t_2$ the curves are clearly self-similar when expressed in terms of $r_\parallel/(t - t_0)$.

Now a linear growth in l_z^I is not, in itself, proof that the large eddies grow by inertial wave propagation. However, as discussed in § 2, self-similarity of the correlations when expressed in terms of $r_\parallel/\Omega(t - t_0)$ does provide strong support for eddy growth by linear wave propagation. Just such a collapse on Ω is shown by figure 12, where the results from the two rotation rates and $M = 32$ mm are plotted for $t_1 < t < t_2$. In figure 12(a), $r_\parallel$ is normalized by $(t - t_0)$, whereas in figure 12(b), $r_\parallel$ is normalized by $2\Omega(t - t_0)$. When the rotation rate is not taken into account, each experiment collapses onto itself, but the inclusion of Ω allows both experiments to collapse to a single curve. A similar collapse could also be seen for $M = 50$ mm.

4.2. *Two-point correlations based on vorticity*

Whilst pearlescence can provide details of the size of the large-scale eddies, it cannot provide information on either the velocity or vorticity fields. To obtain these measurements via PIV, we seeded the water with Pliolite particles and then repeated the experiments in the previous section. Figure 13 shows a typical vorticity field at $2\Omega t = 31.4$ in one of the $\Omega = 1.94$ rad s^{-1} experiments. As the vorticity of the turbulence (here low-pass-filtered to the scale of the spacing of the interrogation windows) is far more intense than any residual background recirculation (in the rotating frame), autocorrelations based on the horizontal vorticity component, ω_x, are used to quantify the large-scale dynamics. For convenience we shall also use ω_x to evaluate the Rossby number, such that $Ro = \omega_{\text{r.m.s.}}/2\Omega$, where $\omega_{\text{r.m.s.}}$ is the root mean square of the integral scale vorticity ω_x.

As in § 4.1, let us begin by considering the integral scale, l_z^ω, which is plotted in figure 14. These are now derived from the vorticity autocorrelation $\langle \omega_x \omega_x' \rangle / \langle \omega_x^2 \rangle$ and agree well with the integral scales measured in the pearlescence experiments. Once again we see that, when rotation is present, the development of the flow can be divided into two distinct periods. These periods will be defined by τ_1 and τ_2 which are analogous to t_1 and t_2 in § 4.1. During the initial period, $t < \tau_1$, the Rossby number is

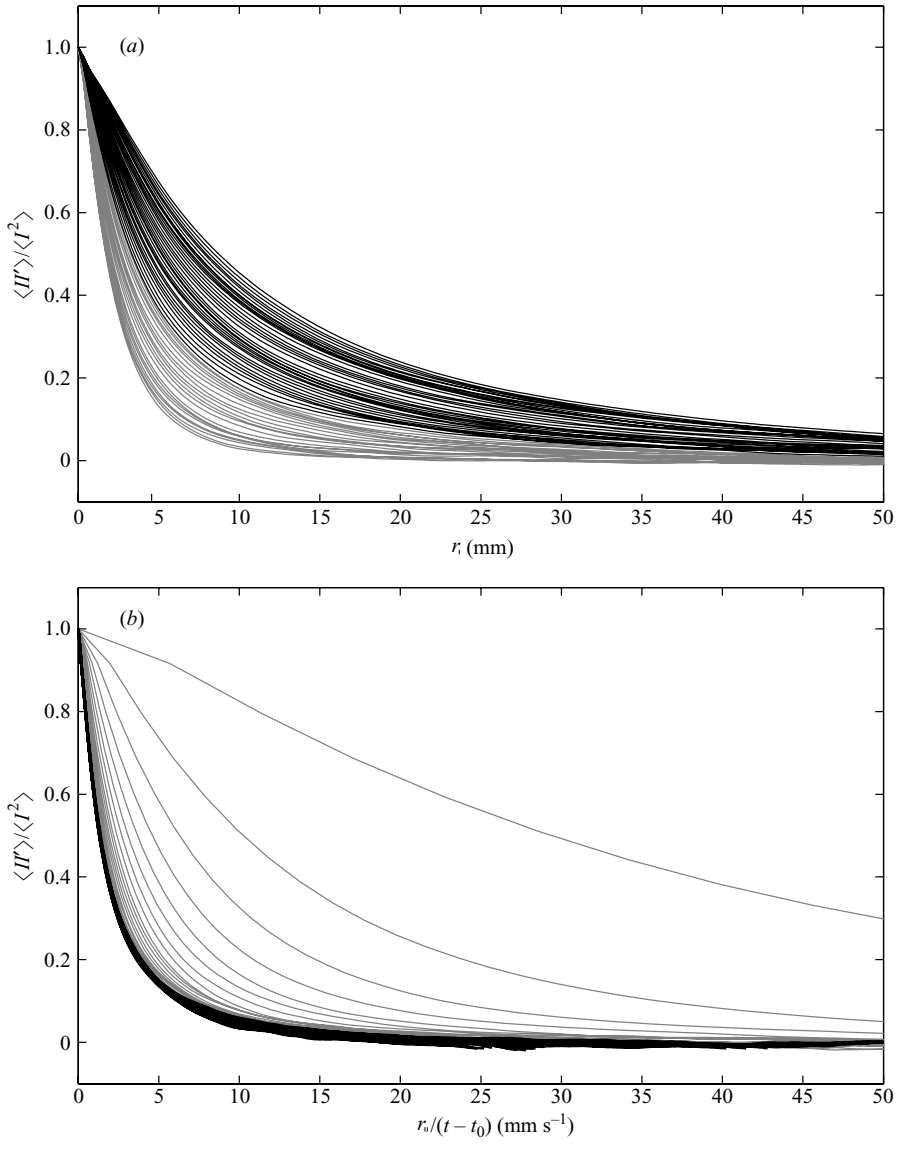

FIGURE 11. Pearlescence correlation curves for $M = 32$ mm, $\Omega = 1.94$ rad s^{-1}: —, $t < t_1$; —, $t_1 < t < t_2$. (*a*) plotted against $r_\parallel$, (*b*) $r_\parallel$ normalized by $(t - t_0)$.

of the order of unity, and both nonlinear dynamics and the Coriolis force influence the turbulence. In the second period, $\tau_1 < t < \tau_2$, the integral scale grows at a constant rate. This coincides with the results in § 4.1, and is consistent with linear inertial wave propagation elongating the large-scale eddies along the rotation axis. The variation of the Rossby number during these two periods is plotted in figure 15, and the times $t = \tau_1$, when the integral scale begins to grow at a constant rate, are shown in table 3. It is evident that the linear growth in l_z^ω occurs around a value of $Ro \sim 0.4$, which is close to the value of 0.2 observed by Hopfinger *et al.* (1982, 1983). We anticipate that, the

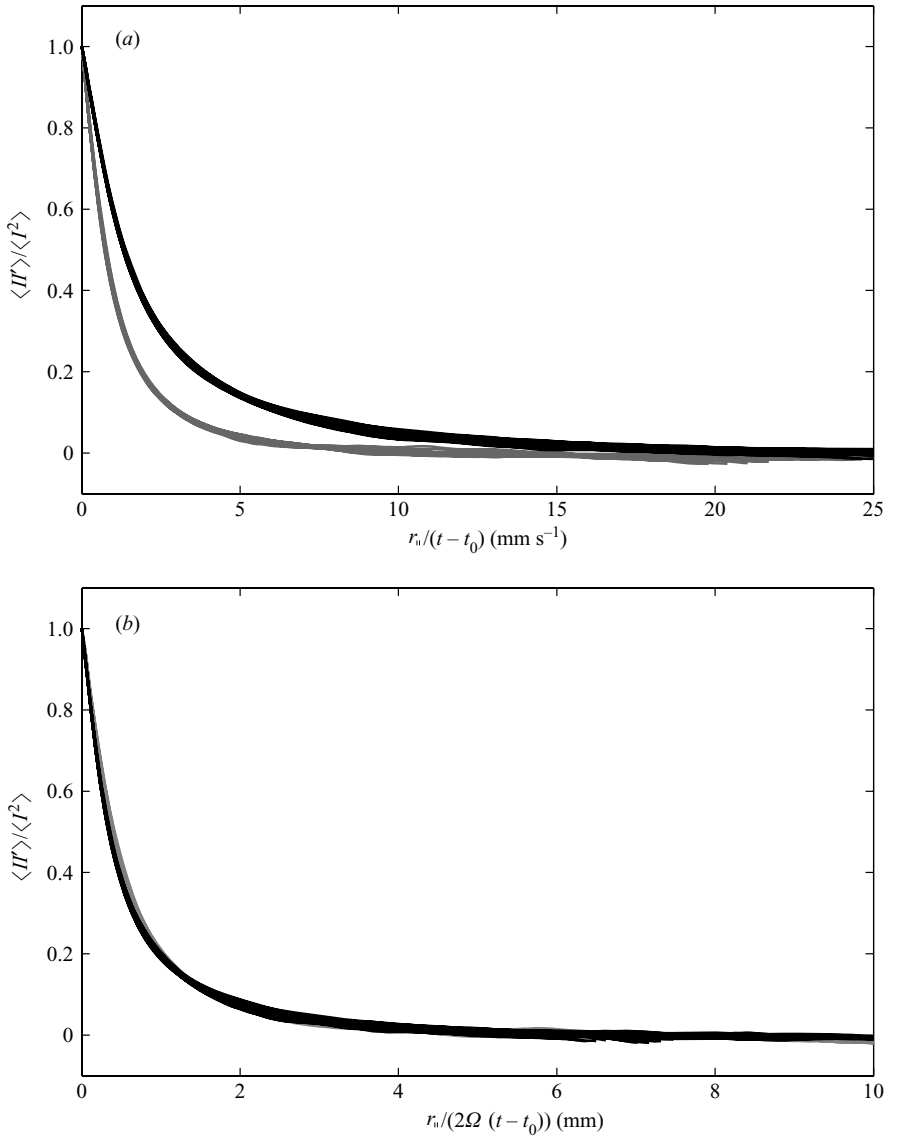

FIGURE 12. Pearlescence correlation curves for $(t_1 < t < t_2)$: —, $M = 32$ mm, $\Omega = 0.94$ rad s^{-1}; —, $M = 32$ mm, $\Omega = 1.94$ rad s^{-1}. (*a*) $r_{\parallel}$ normalized by $(t - t_0)$, (*b*) $r_{\parallel}$ normalized by $2\Omega(t - t_0)$.

modest difference between our value of critical *Ro* and that of these earlier papers is largely due to differences in the experimental configurations. (The earlier experiments were strongly inhomogeneous and continually forced.) However, we cannot entirely rule out some influence of the Reynolds number.

Figure 16(*a*) shows the normalized correlation curves that were used to evaluate l_z^{ω} in figure 14. For $\tau_1 < t < \tau_2$, a normalization of $r_{\parallel}$ by $(t - \tau_0)$ should yield an approximately self-similar collapse, and indeed just such a collapse is shown in figure 16(*b*) for both rotation rates and bar sizes. As mentioned in the previous section, the linear growth of the integral scales is not, in itself, proof that linear inertial wave

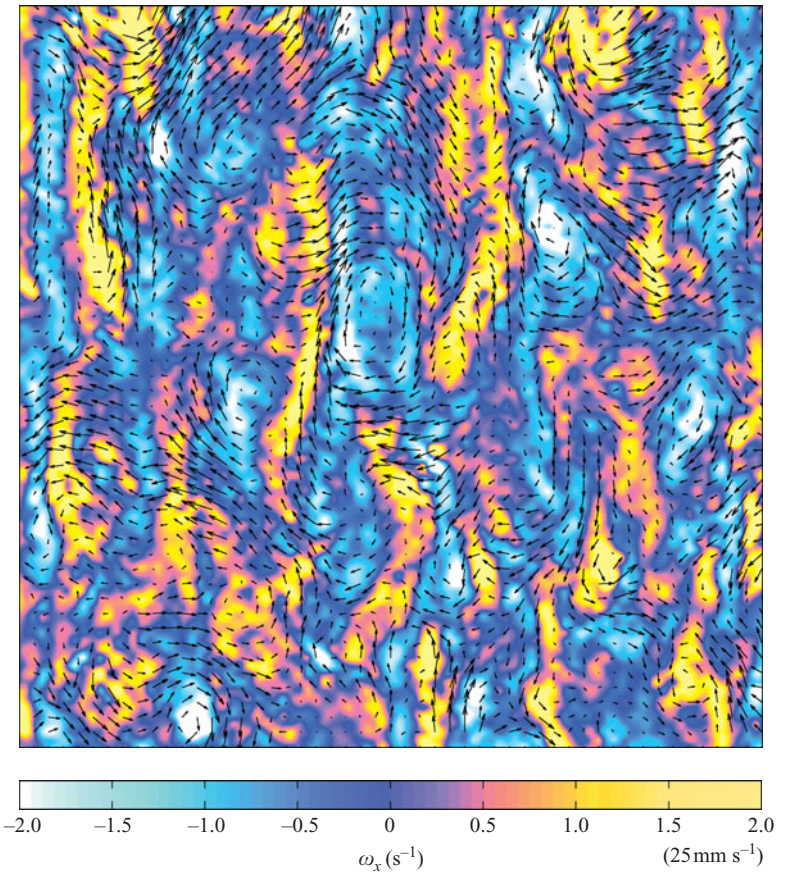

FIGURE 13. A typical vorticity field for the turbulence at $2\Omega t = 31.4$ with $M = 32$ mm and $\Omega = 1.94$ rad s^{-1}. The image is 25 cm square.

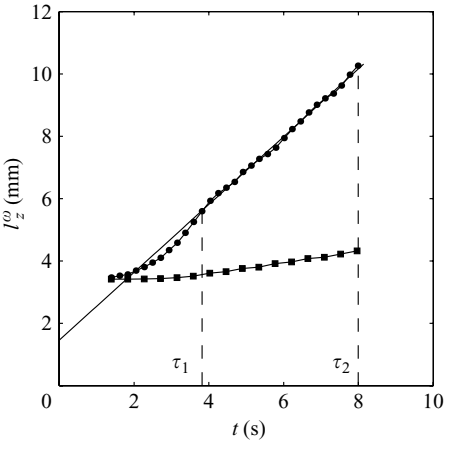

FIGURE 14. The growth of the integral scale from PIV experiments: ■, $M = 32$ mm, $\Omega = 0$ rad s^{-1}; ●, $M = 32$ mm, $\Omega = 1.94$ rad s^{-1}.

Symbol	Ω (rad s^{-1})	M (mm)	Ro ($t = \tau_1$)	$2\Omega\tau_0$	$2\Omega\tau_1$	$2\Omega\tau_2$	2Ω ($\tau_2 - \tau_1$)
◆	0.94	32	0.38	−8.4	13.4	23.3	9.9
◇	0.94	50	0.42	−3.0	14.6	20.8	6.2
●	1.94	32	0.36	−5.2	14.8	31.4	16.6
○	1.94	50	0.40	−2.0	10.6	17.8	7.2

TABLE 3. The time during which the correlations based on ω_x. The integral scale l_z^ω grows linearly during the interval $\tau_1 < t < \tau_2$, and τ_0 is the virtual origin in time.

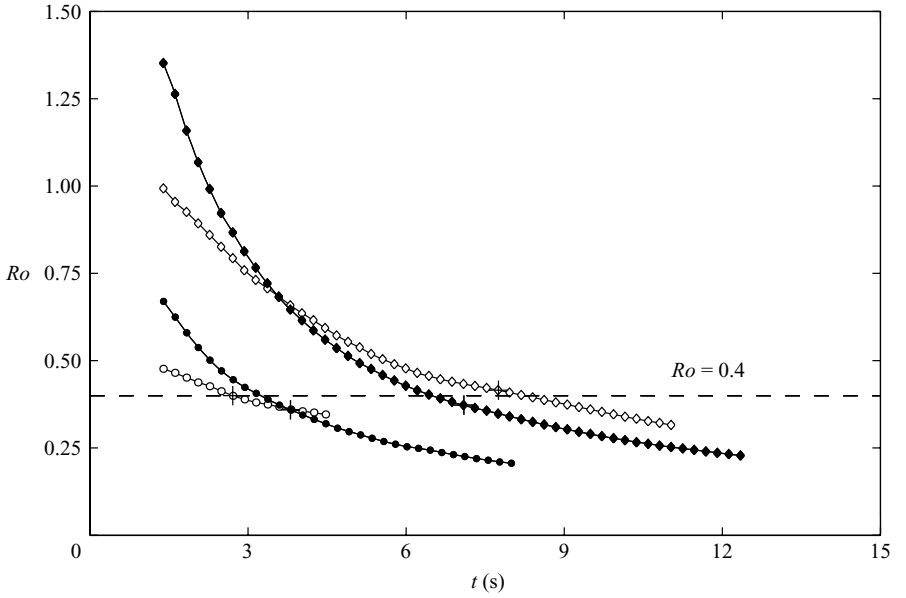

FIGURE 15. The variation of the Rossby number, Ro, with time. The symbols are defined in table 3 and + indicates where $t = \tau_1$.

propagation is the cause for the growth in l_z^ω. However, if the autocorrelation curves scale on $\Omega(t - \tau_0)$, then we have reasonable support for the hypothesis that the large-scale eddies evolve through linear wave propagation. As with the pearlescence results, just such a collapse on Ω^{-1} can be seen for each bar size in figure 17(*a*).

We now consider one final normalization, based on the size of the large-scale eddies. According to expression (1.2), l_z^ω should scale with the initial integral scale, which is set by the bar size of the grid. Consequently, a normalization of $r_\parallel$ by $\Omega(t - \tau_0)b$ should collapse the autocorrelations of all the rotating experiments. Figure 17(*b*) shows that this is indeed the case and provides strong support for the idea that linear wave propagation is the cause of the growth in l_z^ω.

5. Statistics in a horizontal plane

5.1. *Symmetry breaking*

So far we have focused on the axial elongation of eddies. Whilst correlations have allowed us to gain some insight into the manner in which these structures form, we have not yet seen the symmetry-breaking properties of rotating turbulence. This is a matter we shall now address. It is often reported that the columnar structures

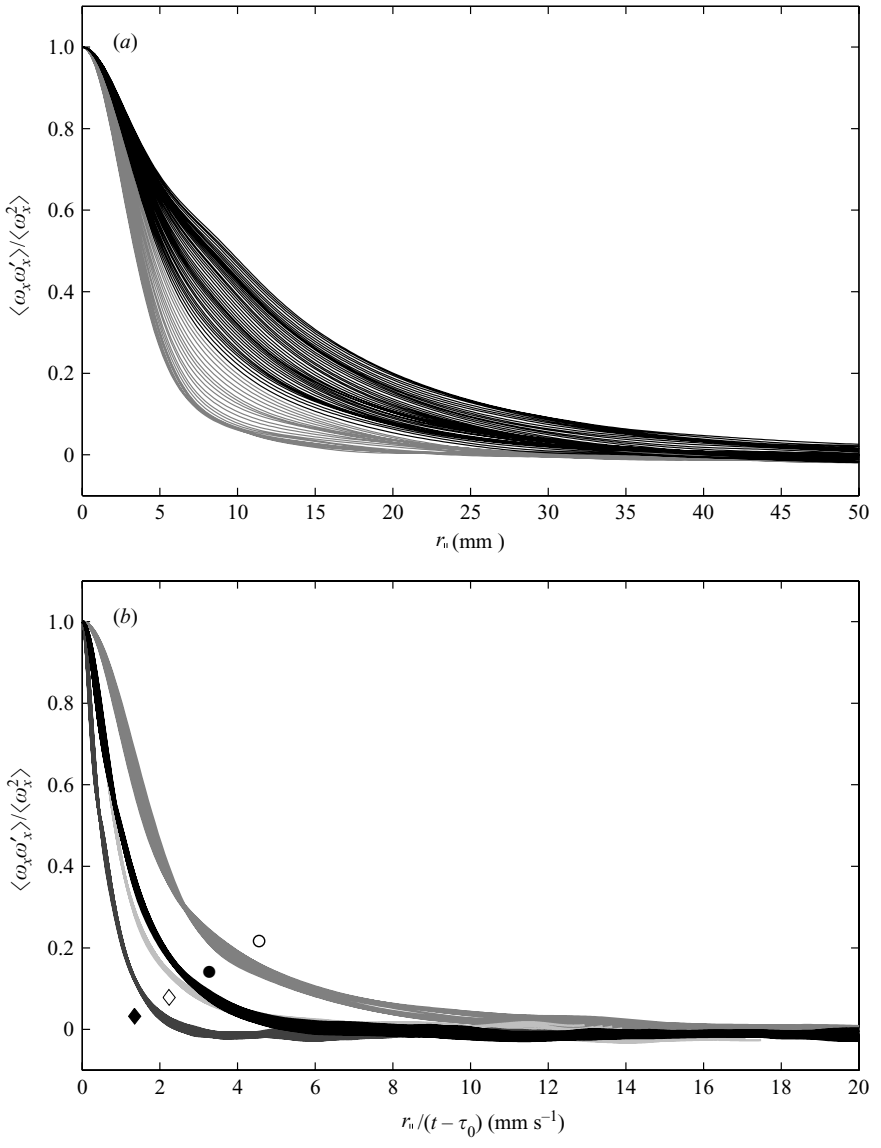

FIGURE 16. (*a*) Vorticity correlation curves for $M = 32$ mm, $\Omega = 1.94$ rad s^{-1}: —, $t < \tau_1$; —, $\tau_1 < t < \tau_2$. (*b*) Vorticity correlation curves corresponding to four different configurations of Ω and b for $\tau_1 < t < \tau_2$. Here $r_{\shortparallel}$ is normalized by $(t - \tau_0)$ and the symbols are defined in table 3.

which form are predominantly cyclonic. This was first observed in the experiments on inhomogeneous turbulence by Hopfinger *et al.* (1982, 1983). By oscillating a grid in the bottom of a rotating tank of water, columnar structures formed and the majority rotated in the same direction as the background rotation. This has since been followed up by studies of homogeneous turbulence, where a dominance of cyclones has also been observed (see, for example, Bartello *et al.* 1994 and Morize *et al.* 2005).

The processes that create this asymmetry are not yet fully understood. One explanation is furnished by Bartello *et al.* (1994). They begin by using Rayleigh's stability criterion to show that when a background rotation is present, an axisymmetric

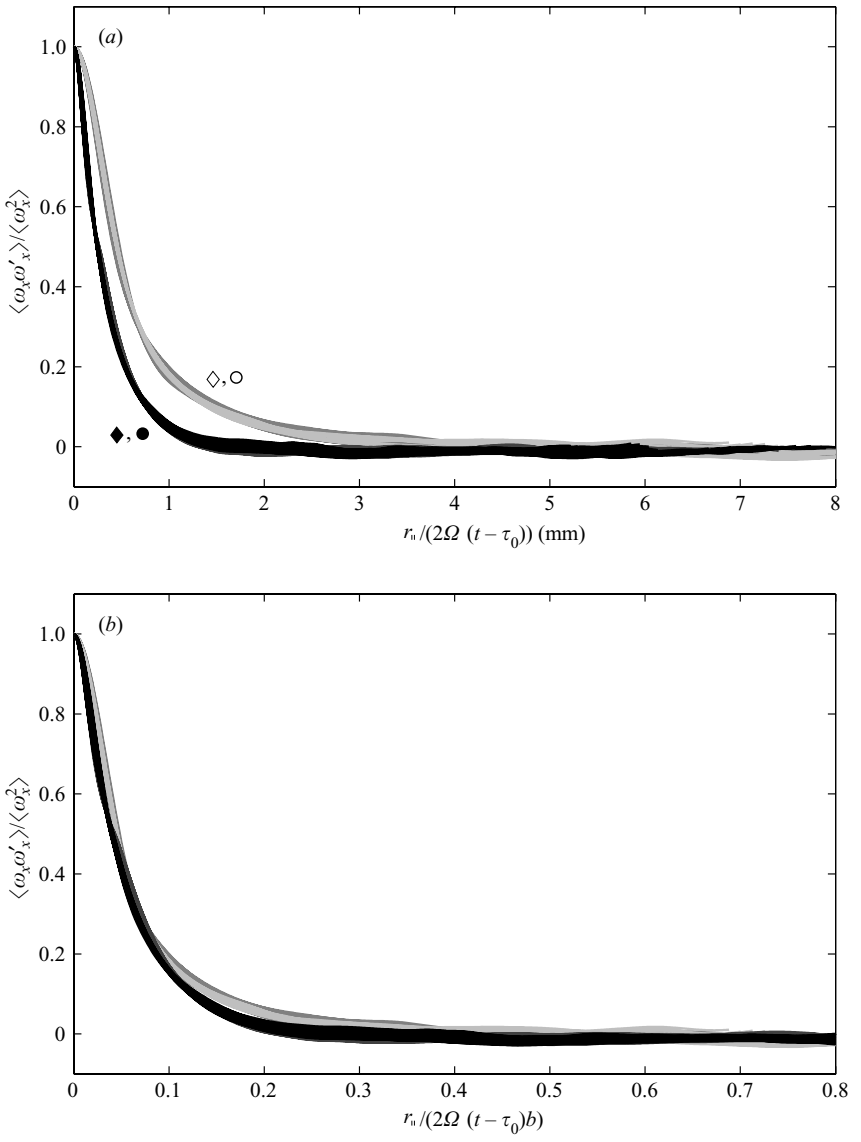

FIGURE 17. Vorticity correlation curves corresponding to four different configurations of Ω and b for $\tau_1 < t < \tau_2$. The symbols are defined in table 3. (*a*) $r_\parallel$ normalized by $2\Omega(t - \tau_0)$, (*b*) $r_\parallel$ normalized by $2\Omega(t - \tau_0)b$.

columnar vortex is unstable in regions where $\omega_z < -2\Omega$. In turn, a counter-rotating vortex is more likely to be unstable than a co-rotating vortex when $Ro \sim 1$. The authors then suggest that this result is relevant to rotating turbulence. As a field of turbulence decays, it is proposed that both cyclonic and anti-cyclonic structures form. As counter-rotating vortices are generally unstable, it is inferred that the anti-cyclones are more susceptible to background perturbations. Consequently, more of the anti-cyclones break up and the symmetry of the flow is broken. There are, however, other possible explanations for the asymmetry. For example, Gence & Frick (2001) considered fully developed, isotropic turbulence which is suddenly subjected

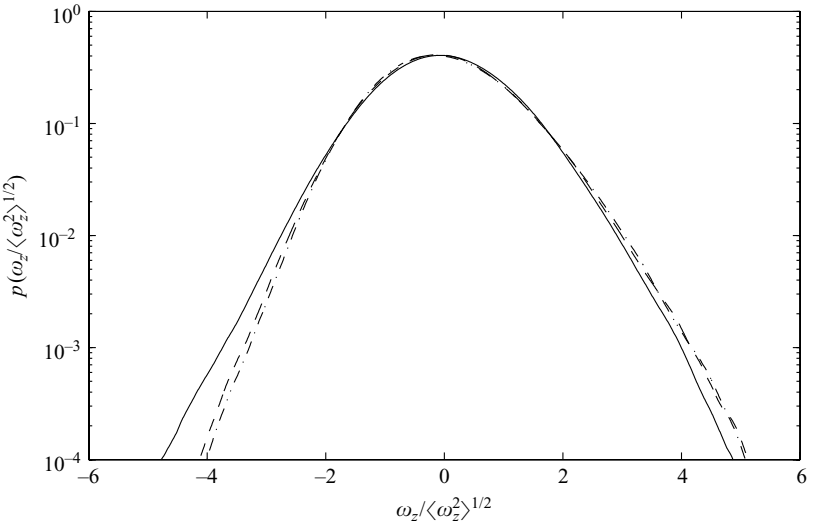

FIGURE 18. Probability density function of the axial vorticity, ω_z: —, initial distribution; —·—, $t = \tau_1$; ——, $t = \tau_2$.

to background rotation. They showed that, at the moment at which the rotation is applied,

$$\frac{\partial}{\partial t}\langle\omega_z^3\rangle = 0.4\Omega\langle\omega_i\omega_j S_{ij}\rangle,$$

where S_{ij} is the rate-of-strain tensor. Since $\langle\omega_i\omega_j S_{ij}\rangle > 0$ in fully developed, isotropic turbulence, the vorticity skewness must become positive, which is taken to be indicative of the dominance of cyclones. Other related explanations have been offered, such as the stretching of absolute vorticity, which favours cyclones. To date, there is no consensus as to which, if any, of these explanations is correct.

To investigate this asymmetry, the experiments in § 4 were repeated with a horizontal lightsheet illuminating the mid-section of the tank. The velocity fields within this plane were then determined by PIV and the degree of asymmetry is viewed using both the probability density function, $p(\omega_z)$, and the skewness,

$$S(\omega_z) = \frac{\langle\omega_z^3\rangle}{\langle\omega_z^2\rangle^{3/2}}. \tag{5.1}$$

Both of these measures have been used in the previous studies of Bartello *et al.* (1994), Ruppert-Felsot *et al.* (2005) and Morize *et al.* (2005). From the plot of $p(\omega_z)$ for $M = 32$ mm and $\Omega = 1.94$ rad s^{-1} in figure 18, it is clear that whilst initially $p(\omega_z)$ is very close to being symmetric, the symmetry of flow is indeed broken. As time progresses, $p(\omega_z)$ increases for positive vorticity, and consequently decreases for negative vorticity.

This asymmetry is also shown in figure 19 where the skewness has been plotted for all of the rotating experiments. In all cases, the skewness is positive, suggesting that cyclones are the predominant structures. In line with previous investigations we find that S grows as $S \sim (2\Omega t)^n$, where Morize *et al.* (2006) suggest $n \sim 0.7$, a result which is not inconsistent with our data. We also observe that for most of our experiments S tends to saturate at around $t = \tau_1$. This saturation in S is also observed in Morize *et al.* (2006).

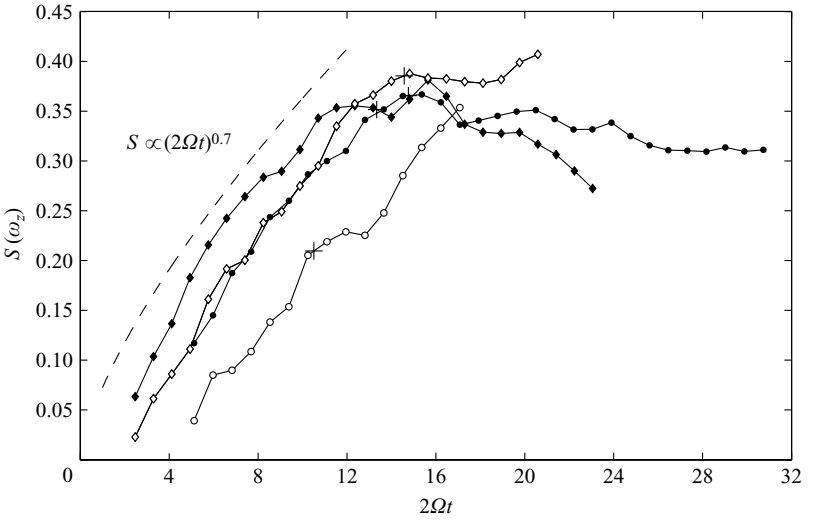

FIGURE 19. The growth of the skewness $S(\omega_z)$. Symbols are defined in table 3 and + indicates where $t = \tau_1$.

5.2. *Energy decay*

It is widely accepted that turbulence decays at a slower rate when background rotation is present. Furthermore, this slower decay rate is often linked to the growth of columnar eddies (see, for example, Jacquin *et al.* 1990). The reasoning for this is as follows. In classical non-rotating turbulence, the majority of energy is contained in the large-scale eddies. As the flow decays, energy is passed from these large scales, via the Richardson cascade, down to the smallest scales where it is dissipated by viscosity. The rate at which energy is passed down the cascade, and hence the dissipation rate of the turbulence, is governed by the large-scale turnover time, l/u. In rotating turbulence, on the other hand, we have seen that the large-scale dynamics behave differently, forming columnar structures that persist for far longer than their typical turnover time. Consequently, energy is retained by these stable structures and restricts the transfer of energy to the smaller scales. In turn the dissipation rate is also reduced, a result which is confirmed by the experiments of Jacquin *et al.* (1990) and Bartello *et al.* (1994).

In our experiments, we also see that increasing the background rotation reduces the rate of dissipation. This is shown by figure 20, which plots the variation of $\langle \boldsymbol{u}_\perp^2 \rangle$ in the horizontal plane. To quantify the decay of energy, experimental data are normally fitted with a power law function

$$u^2 = A(t - t^*)^{-n},$$

where t^* is a virtual origin in time. In these experiments, measurements are conducted over modest periods of time, which leads to uncertainty when evaluating t^* and hence the decay exponent n. Consequently, we shall not estimate n but simply note that for both mesh sizes, increasing the rotation rate inhibits the energy decay by an amount similar to that observed by Jacquin *et al.* (1990). The dashed lines on the graphs correspond to

$$\frac{\langle \boldsymbol{u}_\perp^2 \rangle}{\langle \boldsymbol{u}_\perp^2 \rangle_0} = \left[1 + c \frac{\varepsilon_0 (t - t^*)}{\frac{1}{2} \langle \boldsymbol{u}^2 \rangle_0} \right]^{-1/c}, \tag{5.2}$$

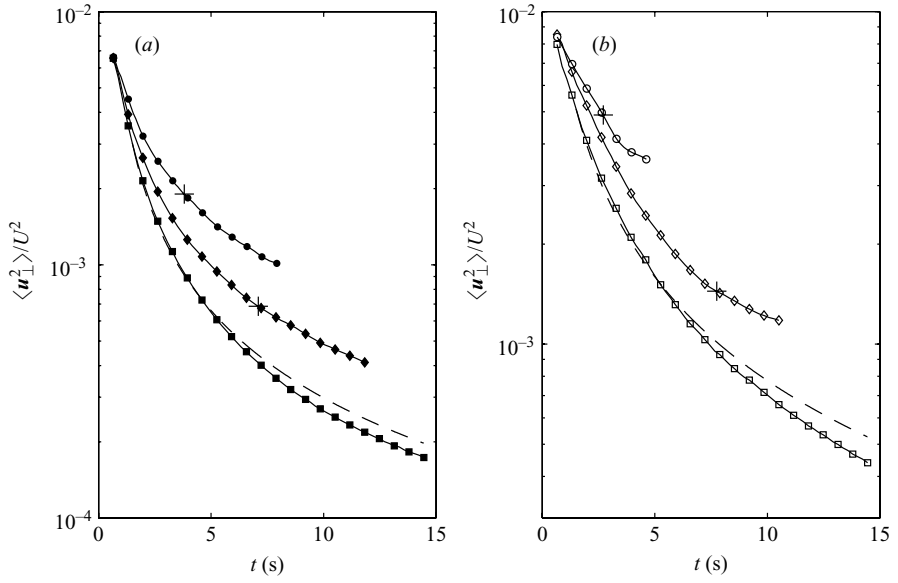

FIGURE 20. Decay of $\langle \boldsymbol{u}_\perp^2 \rangle$ within the horizontal plane. Rotating cases are plotted for times $t < \tau_2$ and + indicates where $t = \tau_1$. (*a*) $M = 32$ mm with: ■, $\Omega = 0$; ◆, $\Omega = 0.94\,\mathrm{rad\,s^{-1}}$; ●, $\Omega = 1.94\,\mathrm{rad\,s^{-1}}$, (*b*) $M = 50$ mm with: □, $\Omega = 0$; ◇, $\Omega = 0.94\,\mathrm{rad\,s^{-1}}$; ○, $\Omega = 1.94\,\mathrm{rad\,s^{-1}}$. Dashed lines correspond to (5.2).

where ε_0 is the dissipation rate, $-\frac{1}{2}\,\mathrm{d}\langle \boldsymbol{u}^2 \rangle_0 / \mathrm{d}t$, when the grid has come to rest. This is the standard one-point closure prediction for non-rotating, decaying grid turbulence at high *Re*. (In these models c is given the standard value of 0.92 based on grid turbulence data.) It is reassuring that our data and the curves are reasonably close.

It is interesting to note that all of the curves for rotating turbulence remain smooth at $t = \tau_1$ (indicated by + marks in figure 20) with no obvious change in their form. This is in contrast to our measurements of other statistics of the flow. Although the reason for this is uncertain, we note that dissipation is an essentially nonlinear process and so the role of linear dynamics influencing the development of the largest scales of the flow will only indirectly affect the Richardson cascade, leading to a gradual rather than an abrupt change in the rate of dissipation.

6. Conclusions

Our laboratory experiments have focused on rotating turbulence with $Ro \sim 1$. In this regime, we have observed that the large scales, which are initially dominated by inertia, form columnar eddies aligned with the rotation axis. We have studied this formation using two-point, one-time correlations in the axial direction. Both reflected light intensity and the integral-scale vorticity have been used for the correlations and the results of the two techniques are in agreement.

In both cases the axial integral scale, determined from the correlation curves, grows linearly with time once $Ro < 0.4$. During this period of linear growth the two-point correlations can be collapsed when $r_\parallel$ is normalized by $\Omega t b$. These findings are consistent with columnar structure formation through linear inertial wave propagation, and suggests that the proposal of DSD can be extended from inhomogeneous to homogeneous turbulence.

As well as viewing the columnar structures, we have observed other, well-accepted, properties of rotating turbulence. For all rotating experiments a predominance of cyclones has been seen, and the skewness plots which describe this predominance are in line with previous studies. (See, for example, Morize *et al.* 2005.) The skewness initially grows as $(2\Omega t)^n$ and saturates at a value of ~ 0.4. There is also clear evidence that the rate of energy decay is slowed by background rotation. As rotation increases, more energy is retained by stable large-scale structures and thus prevented from cascading to small scales.

REFERENCES

Bartello, P., Metais, O. & Lesieur, M. 1994 Coherent structures in rotating three-dimensional turbulence. *J. Fluid Mech.* **273**, 1–29.

Bracewell, R. N. 1986 *The Fourier Transform and its Applications*, 2nd edn. McGraw-Hill.

Cambon, C., Mansour, N. N. & Godeferd, F. S. 1997 Energy transfer in rotating turbulence. *J. Fluid Mech.* **337**, 303–332.

Cambon, C. & Scott, F. S. 1999 Linear and nonlinear models of anisotropic turbulence. *Annu. Rev. Fluid Mech.* **31**, 1–53.

Dalziel, S. B., Carr, M., Sveen, J. K. & Davies, P. A. 2007 Simultaneous synthetic schlieren and PIV measurements for internal solitary waves. *Meas. Sci. Tech.* **18**, 533–547.

Davidson, P. A. 2007 On the large-scale structure of homogeneous two-dimensional turbulence. *J. Fluid Mech.* **580**, 431–450.

Davidson, P. A., Staplehurst, P. J. & Dalziel, S. B. 2006 On the evolution of eddies in a rapidly rotating system. *J. Fluid Mech.* **557**, 135–144.

Gence, J. N. & Frick, C 2001 Naissance des corrélations triples de vorticité dans une turbulence statistiquement homogène soumise à une rotation. *CR Acad. Sci. Paris* II **329**, 351–356.

Greenspan, H. P. 1968 *Theory of Rotating Fluids*. Cambridge University Press.

Hopfinger, E. J., Browand, F. K. & Gagne, Y. 1982 Turbulence and waves in a rotating tank. *J. Fluid Mech.* **125**, 505–534.

Hopfinger, E. J., Griffiths, R. W. & Mory, M. 1983 The structure of turbulence in homogeneous and stratified rotating fluids. *J. Mech. Theoriq. Appl.* (special issue) **44**, 21–44.

Jacquin, L., Leuchter, O., Cambon, C. & Mathieu, J. 1990 Homogeneous turbulence in the presence of rotation. *J. Fluid Mech.* **220**, 1–52.

Jeffery, G. B. 1922 The motion of ellipsoidal particles immersed in a viscous fluid. *Proc. R. Soc. Lond.* A **102**, 161–179.

Lighthill, J. 1978 *Waves in Fluids*. Cambridge University Press.

McKenna, S. P. & McGillis, W. R. 2004 Observations of flow repeatability and secondary circulation in an oscillating grid-stirred tank. *Phys. Fluids* **16**, 3499.

Morize, C. & Moisy, F. 2006 Energy decay of rotating turbulence with confinement effects. *Phys. Fluids* **18**, 065107.

Morize, C., Moisy, F. & Rabaud, M. 2005 Decaying grid-generated turbulence in a rotating tank. *Phys. Fluids* **17**, 095105.

Morize, C., Moisy, F., Rabaud, M. & Sommeria, J. 2006 On the cyclone–anticyclone asymmetry in decaying rotating turbulence. In *Conference on Turbulence and Interactions TI2006*.

Ruppert-Felsot, J. E., Praud, O., Sharon, E. & Swinney, H. L. 2005 Extraction of coherent structures in a rotating turbulent flow experiment. *Phys. Rev.* E **72**, 016311.

Savas, O. 1985 On flow visualization using reflective flakes. *J. Fluid Mech.* **152**, 235–248.

Townsend, A. A. 1976 *The Structure of Turbulent Shear Flows*. Cambridge University Press.

Waleffe, F. 1993 Inertial transfers in the helical decomposition. *Phys. Fluids* A **5**, 667–685.